AIAA JOURNAL
Vol. 41, No. 10, October 2003

Verification and Validation for Laminar Hypersonic Flowfields, Part 2: Validation

Christopher J. Roy,* William L. Oberkampf,† and Mary A. McWherter-Payne‡
Sandia National Laboratories, Albuquerque, New Mexico 87185

A validation methodology is applied to the laminar Mach 8 flow over a spherically blunted cone. Validation of the overall computational model is performed via surface pressure comparisons with experimental data. Careful attention is paid to the submodels in the computational simulations and the assumptions in the experimental data analysis. The computational submodels for molecular viscosity and thermal conductivity are validated by comparisons to experimental data, whereas the vibrational nonequilibrium submodel is validated by comparing to published results using the vibrational master equation. The thermodynamic state of the hypersonic wind-tunnel nozzle is examined, and arguments are made for the presence of a significant amount of vibrational nonequilibrium in the tunnel. After extensive investigation, a 1.4% error was discovered in the freestream static pressure originally reported in the experiment. Accounting for this error, along with the experimental uncertainty and estimated numerical error, agreement was found for surface pressure within 1.5%. The remaining errors are likely due to flowfield nonuniformities in the tunnel, which are estimated using tunnel pitot calibration data and the method of characteristics.

Nomenclature

C_p	=	specific heat at constant pressure, J/kg · K
C_v	=	specific heat at constant volume, J/kg · K
e	=	specific internal energy, J/kg
$\dot{e}$	=	specific internal energy rate of change, J/(kg · s)
k	=	thermal conductivity, W/m · K
P	=	continuum breakdown parameter
Pr	=	Prandtl number, 0.71
p	=	pressure, N/m^2
R	=	specific gas constant, R_u/W, J/kg · K
R_N	=	nose radius, 0.00508 m
R_u	=	universal gas constant, 8314.34 J/kmol · K
T	=	translational–rotational temperature, K
T_{vib}	=	vibrational temperature, K
W	=	molecular weight, 28.013 kg/kmol for N_2
x	=	axial coordinate, m
y	=	radial coordinate (Cartesian for three dimensions), m
z	=	Cartesian coordinate for three dimensions, m
γ	=	ratio of specific heats, C_p/C_v
δ	=	boundary-layer thickness, m
θ_{vib}	=	characteristic vibrational temperature K, 3390 K for N_2
μ	=	absolute viscosity, N · s/m^2
ρ	=	density, kg/m^3
$\bar{\rho}$	=	molar density, kmol/m^3
τ	=	characteristic vibrational relaxation time, s
ϕ	=	Landau–Teller acceleration factor τ_{LT}/ϕ

Subscripts and Superscripts

LT	=	Landau–Teller
ref	=	reference value
vib	=	vibrational energy mode
$*$	=	equilibrium value
∞	=	freestream value

Received 29 July 2002; revision received 26 March 2003; accepted for publication 4 April 2003.

*Senior Member of Technical Staff, P.O. Box 5800; currently Assistant Professor, Department of Aerospace Engineering, Auburn University, 211 Aerospace Engineering Building, Auburn University, AL 36849-5338; cjroy@eng.auburn.edu. Senior Member AIAA.

†Distinguished Member of Technical Staff, Mail Stop 0828, P.O. Box 5800. Associate Fellow AIAA.

‡Principal Member of Technical Staff, Mail Stop 0825, P.O. Box 5800. Senior Member AIAA.

Introduction

ALTHOUGH validation of simulation models can be viewed very broadly,[1] we will take the more restricted view that validation consists of comparing a verified numerical solution with experimental data for which experimental uncertainty is estimated. Validation can be performed for either the submodels, for example, transport models, equation of state models, thermodynamic models, turbulence models, etc., or for the overall computational model, that is, simulation code, through comparisons with experimental data. Once model validation has been performed for a given set of conditions, the measure of agreement between the model and the experiment can be compared with simulation requirements so that conclusions can be drawn regarding the adequacy of the proposed mathematical models for the intended application. The simulation tool can then be extended to conditions and configurations that are sufficiently close in the parameter space to the validation case.

The computational and experimental results presented herein are for a Mach 8, laminar, spherically blunted cone. This configuration was studied experimentally at the Sandia National Laboratories hypersonic wind tunnel facility under the Joint Computational/Experimental Aerodynamics Program (JCEAP). The experimental model had a planar slice on the aft section (parallel to the longitudinal axis), where 10-, 20-, and 30-deg flaps could be mounted. The experimental database consists of both force and moment[2,3] and surface pressure[4,5] measurements. The current paper deals with the validation of the chosen models for studying attached laminar flow at hypersonic Mach numbers. The simulations are generally performed as axisymmetric, with data comparisons limited to regions not influenced by the planar slice. The numerical accuracy of the solutions was carefully addressed in the companion paper.[6]

The main goal of the current work is to present, by way of example, the different steps involved in the validation process. These steps include detailed analysis of the uncertainty and error found both in the experiment and in the computations. The remainder of this paper is organized as follows. A brief description of the experimental test conditions is given, followed by a discussion of the governing equations and thermodynamic models used. Computational submodel validation results are presented, which include calculations of the hypersonic nozzle used to determine the state of the vibrational

excitation in the wind-tunnel test section. Results are then given that compare the numerically accurate computational results[6] for surface pressure to experimental data. Finally, discrepancies between the experimental and computational results are addressed, and conclusions are drawn.

Experimental Description

The simulations presented herein are compared to surface pressure measurements collected under the JCEAP at the Sandia National Laboratories hypersonic wind tunnel facility.[4,5] The wind tunnel is a blowdown-to-vacuum configuration and has capabilities for Mach 5, 8, and 14 flow. The Mach 8 nozzle uses dry nitrogen (99.999% pure) with a series of heater screens upstream of the nozzle throat to prevent nitrogen condensation in the test section. The tunnel cross-section is rectangular (0.127×0.178 m) in the plenum and transitions to a circular cross section approximately 0.1 m upstream of the nozzle throat.[2] The circular test section, located approximately 2 m downstream of the nozzle throat, has a diameter of 0.35 m.

The JCEAP model is a 10-deg half-angle spherically blunted cone with a length of 0.2639 m and a nose radius of 0.00508 m. A planar slice is located on the aft section beginning at 0.7 of the length of the body where 10-, 20-, and 30-deg flaps can be mounted (Fig. 1). The mountable flaps offer a wide range of flow complexity from laminar attached flow to laminar separated flow. The model contains a total of 96 pressure ports located circumferentially around the body at various axial stations, in addition to a number of ports on the slice and flaps. Data were taken at various angles of attack, roll angles, and at two different axial locations in the tunnel. After varying these parameters and conducting numerous repeat runs, a statistical method was employed to improve the estimate of the mean, as well as to improve the estimate of the experimental uncertainty.[4,5] The experimental uncertainty comes from various sources including tunnel flow nonuniformity, model imperfections, positional uncertainty, instrumentation uncertainty, and run-to-run variations in freestream conditions.

Table 1 Test conditions for JCEAP surface pressure experiments

Flow parameter	Mean value	One standard deviation, %
Freestream Mach number	7.841	0.032
Stagnation pressure	2.4724×10^6 N/m^2	2.1
Stagnation temperature	632.8 K	2.1
Freestream static pressure	286.8 N/m^2 (290.9 N/m^2)[a]	1.4
Freestream static temperature	47.7 K	None given
Freestream unit Reynolds number	6.88×10^6/m	3.7

[a]An error was found in the nominal freestream static pressure reported in Ref. 4; the corrected value is shown in parentheses.

The test conditions are given in Table 1 along with run-to-run variations for one standard deviation. The stagnation pressure is measured in the plenum, and the stagnation temperature is determined from the plenum pressure and a mass balance between the nozzle throat and a control valve located upstream of the heaters. The tunnel Mach number was calibrated by measuring the local pitot pressure using a rake in the test section. Assuming thermal equilibrium and isentropic flow in the nozzle, the Mach number, static pressure, and Reynolds number in the test section were computed using the measured quantities. The validity of the thermal equilibrium assumption will be assessed later.

Flowfield Model

Governing Equations

The computational fluid dynamics code used in the current work is SACCARA, the Sandia advanced code for compressible aerothermodynamics research and analysis. The SACCARA code was developed from a parallel distributed memory version[7,8] of the INCA code,[9] originally developed at Amtec Engineering. The SACCARA code employs a massively parallel distributed memory architecture based on multiblock structured grids. The Navier–Stokes equations are solved for conservation of mass, momentum, global energy, and vibrational energy (where applicable) in finite volume form. The viscous terms are discretized using central differences. The SACCARA code has two options for determining the inviscid interface fluxes, the Steger–Warming flux vector splitting scheme[10] and Yee's symmetric total variational diminishing TVD scheme.[11] Second-order spatial accuracy is obtained with the former via MUSCL extrapolation of the primitive variables, whereas the latter is nominally second order in smooth regions of the flow. Both schemes employ a flux limiter that reduces to first-order spatial accuracy in regions with large second derivatives of pressure and temperature. The effects of this limiting on the solution as the grid is refined are discussed in detail in Ref. 6.

Unless otherwise stated, all results presented herein use a second-order Steger–Warming[10] flux scheme and assume calorically perfect gas ($\gamma = 1.4$) flow of nitrogen. The boundary conditions are assumed

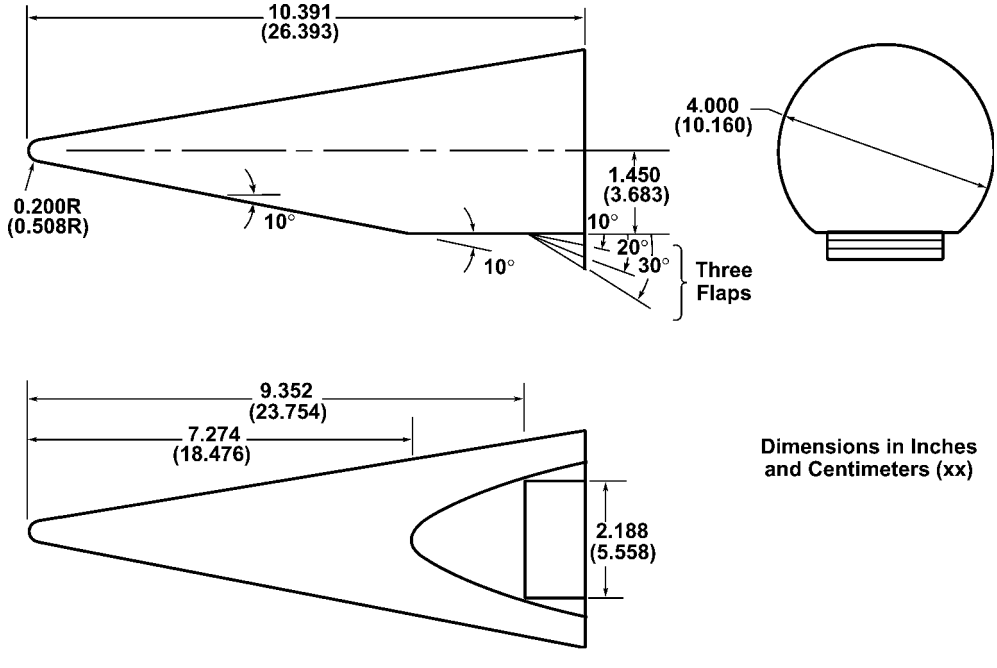

Fig. 1 JCEAP model geometry.

to be fixed at the values reported in Table 1, and a constant wall temperature of 316.7 K was used as suggested in Ref. 12. The simulations are run using a single 400-MHz processor of a Sun Enterprise 10000 shared-memory machine unless otherwise noted. The solutions assume axisymmetric flow to reduce the computational effort, with the exception of a single three-dimensional calculation performed to test the axisymmetric assumption in the presence of the planar slice. Comparisons with the JCEAP experimental data are, thus, limited to data on the conical regions of the model only.

Thermodynamic Models

Calorically Perfect Gas

For a calorically perfect gas, the specific heats are constant. If the ideal gas assumption is made, then the equation of state and energy–temperature relation are expressed as

$$p = \rho(\gamma - 1)e \tag{1}$$

$$T = (\gamma - 1)e/R \tag{2}$$

respectively. For diatomic nitrogen below 300 K, the ratio of specific heats γ is constant at 1.4. Thermally frozen flow can occur at higher temperatures when the thermal relaxation timescales are much larger than the flow residence timescales and may be observed in compressive flows such as shock waves at low pressures, or in rapidly expanding flows. In a thermally frozen flow, the calorically perfect gas assumption is valid provided the correct value of gamma is employed ($\gamma = 1.4$ for diatomic nitrogen).

Thermal Equilibrium

As the temperature increases, the vibrational internal energy mode can be excited. If there is sufficient flow residence time for the internal energy modes to equilibrate, then the specific heats will increase as the temperature rises. This increase in C_p and C_v results in a net drop in the ratio of specific heats γ as the temperature increases. For a thermally perfect gas in thermal equilibrium, the SACCARA code uses polynomial curve fits[13] for the specific heats, enthalpy, and entropy as functions of temperature only. For flows in thermal equilibrium, the thermal relaxation timescale is assumed to be much smaller than the flow residence timescale.

Thermal Nonequilibrium

For a thermally perfect gas in vibrational nonequilibrium, the vibrational relaxation timescale is, in some region of the flow, of the same order of magnitude as the flow residence timescale. To predict such flows, a separate transport equation for the vibrational energy is solved.[14] The right-hand side (RHS) of the vibrational energy transport equation contains a source term of the Landau–Teller (L–T) form that governs the thermal relaxation process:

$$\text{RHS} = \left[e^*_{\text{vib}}(T) - e_{\text{vib}}(T_{\text{vib}})\right] \Big/ \tau_{\text{LT}} \tag{3}$$

where e^*_{vib} is the equilibrium vibrational energy (evaluated at the translational–rotational temperature) and the Landau–Teller (L–T) relaxation timescale τ_{LT} is found from the correlation of Millikan and White.[15] This formulation for the relaxation timescale is based on a harmonic oscillator model and assumes that the energy is distributed among the vibrational energy levels according to a Boltzmann distribution.

Although the standard L–T vibrational relaxation has been shown to give good agreement with experimental data for compressive flows, as early as the 1960s researchers found evidence that vibrational deexcitation occurred much more rapidly for certain expanding flows than was predicted by L–T theory (see Ref. 16). This accelerated relaxation rate is due to anharmonic effects and non-Boltzmann population distributions in the vibrational energy levels (often referred to as vibrational pumping) and can be expressed in terms of a local acceleration factor[17]:

$$\phi = \dot{e}_{\text{vib}}/\dot{e}_{\text{vib, LT}} \tag{4}$$

which multiplies the standard L–T relaxation rate given in Eq. (3). Ruffin[18] suggests that ϕ is a function of the translational temperature and the T_{vib}/T ratio only. Figure 2 (reproduced from Ref. 18) shows the behavior of the L–T acceleration factor as a function of the T_{vib}/T ratio for three different translational temperatures. The correction factor is near unity for compressive flows ($T > T_{\text{vib}}$) and grows as the T_{vib}/T ratio increases.

Equation of State

The relationship between pressure, density, and temperature in the low-pressure limit is given by the ideal gas equation of state

$$p = \rho RT \tag{5}$$

As the pressure is increased, intermolecular forces cause variations from the ideal gas equation of state. The Beattie–Bridgeman equation of state (see Ref. 19) incorporates the effects of intermolecular forces and can be written as

$$p = R_u T(1 - \varepsilon)\rho^{-2}(1/\bar{p} + B) - A\bar{\rho}^2 \tag{6}$$

where

$$A = A_0(1 - a\bar{\rho}), \qquad B = B_0(1 - b\bar{\rho}), \qquad \varepsilon = c\bar{\rho}/T^3$$

and $\bar{\rho}$ is the molar density. The pressure is in units of newtons per square meter and the constants are given in Table 2 along with associated units. In general, the thermodynamic relationships for energy, enthalpy, and entropy must be modified when the ideal gas assumption is replaced with a more complex equation of state. (See Ref. 20 for details.)

Table 2 Constants for Beattie–Bridgeman equation of state (see Ref. 19)

Constant	Value
A_0, N · m/kmol^2	1.362315×10^5
a, m^3/kmol	0.02617
B_0, m^3/kmol	0.05046
b, m^3/kmol	−0.00691
c, m^{3}K/kmol	4.20×10^5

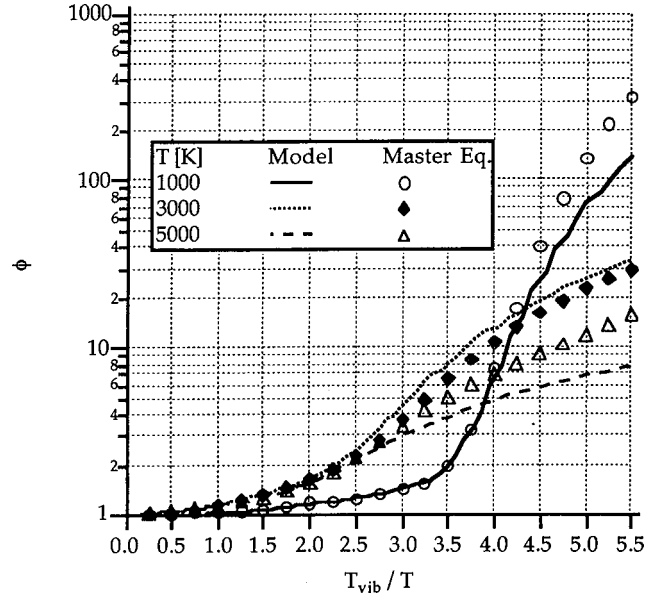

Fig. 2 Comparison of ϕ predicted by Ruffin's simplified anharmonic relaxation model[18] to master equation results for the relaxation of N_2 (reprinted with permission).

Evaluation of Computational Submodels

Before performing overall model validation with the JCEAP surface pressure data, it is important to examine the computational submodels critically as well as the assumptions used in both the simulations and the experiment. The following models and assumptions are evaluated: transport models for viscosity and thermal conductivity, equation of state models, thermodynamic model (vibrational equilibrium vs nonequilibrium), continuum flow assumption, outflow boundary condition model, and axisymmetric flow assumption.

Transport Property Models

A study of the transport properties for nitrogen was undertaken to ensure accuracy over the temperature range of interest (50–650 K). Keyes's model[21] was chosen for the absolute viscosity (in newton seconds per square meter)

$$\mu = \frac{a_0\sqrt{T}}{1 + a[T \cdot 10^{(a_1/T)}]} \tag{7}$$

where $a_0 = 1.418 \times 10^{-6}$, $a = 116.4$, and $a_1 = 5.0$ and was correlated for a range of $90 < T < 1695$ K. Keyes's model is shown in Fig. 3 along with experimental data from Refs. 22 and 23. Also shown in Fig. 3 is Sutherland's law for air and a power law model with

$$\mu = (T/T_{\text{ref}})^{0.74}\mu_{\text{ref}} \tag{8}$$

where $T_{\text{ref}} = 273$ K and $\mu_{\text{ref}} = 1.656 \times 10^{-5}$ Ns/m^2. Good agreement with the data is shown for Keyes's model from 30 to 1000 K. The error in the three models relative to the experimental data is presented in Fig. 4. Keyes's model has a maximum error of 5% found in the low-temperature range. Both Sutherland's law and the power law model show large errors for temperatures below 100 K, whereas the power law model has an 8% error at 1000 K.

The Keyes model for thermal conductivity takes the same form as that for the absolute viscosity; however, the constants are given as $a_0 = 1.8506 \times 10^{-3}$, $a = 77.0$, and $a_1 = 12.0$. Using these constants and the form specified in Eq. (7) gives the thermal conductivity k (watts per meter degrees Kelvin) in the range $273 < T < 773$ K. A comparison of the Keyes model for thermal conductivity with experimental data[22,23] indicates that the model does not perform well at both low and high temperatures (Fig. 5). Better agreement with the data is found by simply assuming a constant molecular Prandtl number of 0.71 along with Keyes's model for viscosity. The error in the thermal conductivity relative to the experimental data is given in Fig. 6. The Keyes model for k shows errors as large as 15% at the high-temperature end, whereas the errors below 150 K may be as large as 50%. Employing the Keyes model for viscosity and assuming a constant Prandtl number results in significantly smaller errors

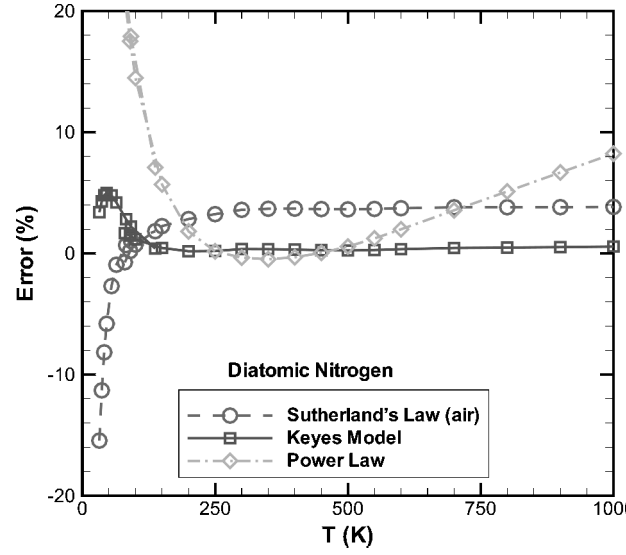

Fig. 4 Error in absolute viscosity for nitrogen relative to experimental data.[22,23]

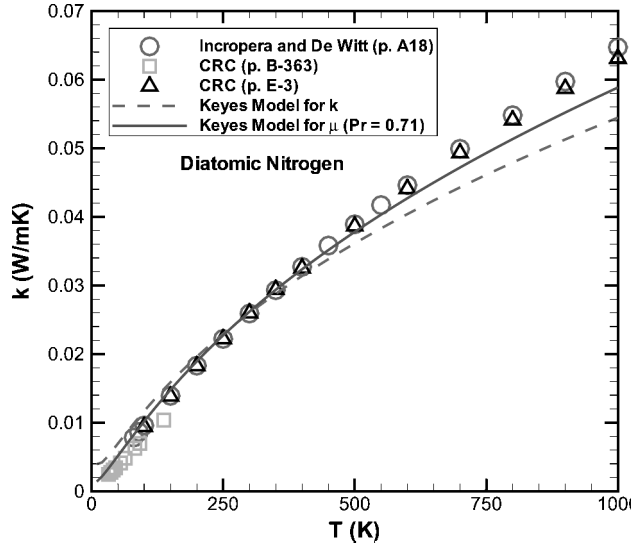

Fig. 5 Thermal conductivity for nitrogen with comparison to experimental data.[22,23]

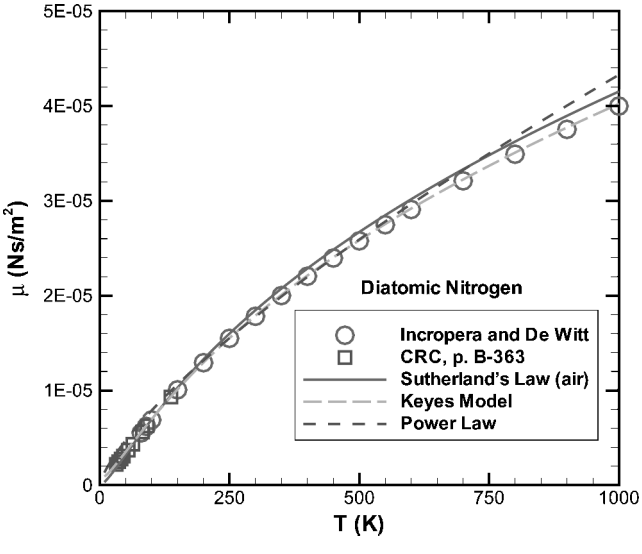

Fig. 3 Absolute viscosity for nitrogen with comparison to experimental data.[22,23]

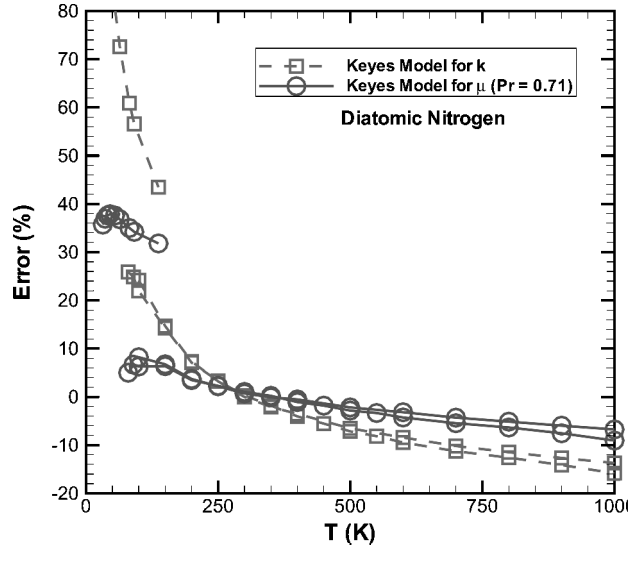

Fig. 6 Error in thermal conductivity for nitrogen relative to experimental data.[22,23]

of 10 and 40% in the higher and lower temperatures, respectively. Whereas the choice of transport models can have a large impact on the skin friction and heat transfer, the choice of the model was found to have negligible effects on the surface pressure.

Equation of State Model

To test the validity of the ideal gas equation of state (5) for the JCEAP conditions, the densities and temperatures from an ideal gas solution were used in an a posteriori calculation of the pressure using the more accurate Beattie–Bridgeman equation of state (see Ref. 19). These pressures were then compared to the ideal gas solution results, with maximum differences of less than 0.05% for the entire flowfield. Thus, the ideal gas equation of state is used for all simulations of the JCEAP sphere–cone geometry.

In the experiment, the freestream conditions (Mach number, Reynolds number, static pressure, and static temperature) were determined from the stagnation pressure, stagnation temperature, and pitot pressure assuming the Beattie–Bridgeman equation of state and thermal equilibrium (see Ref. 19). For the hypersonic nozzle simulations presented in the following section, the ideal gas equation of state is employed. The use of the ideal gas assumption, rather than the more accurate Beattie–Bridgeman equation of state, is appropriate because the nozzle simulations were performed only to determine vibrational excitation levels in the freestream. For reasons discussed later, the nozzle simulations are not expected to match the actual flow in the hypersonic wind tunnel.

Thermodynamic Model

Hypersonic Nozzle Simulations

To determine the thermal state of the hypersonic wind tunnel, that is, vibrational equilibrium vs nonequilibrium, calculations were performed for the Sandia National Laboratories hypersonic wind-tunnel Mach 8 nozzle. These calculations employed the second-order TVD flux scheme and assumed fully turbulent boundary layers on the wind-tunnel walls. The effects of transition and possible relaminarization were, thus, neglected. In addition, the design specifications (prefabrication) were used for the geometry definition, as opposed to postfabrication inspection. One difference between the two was that an inspection of the nozzle throat diameter indicated a diameter of 0.02301 m as compared to 0.02270 m in the design specifications. Although this difference is small (1.37%), it could lead to Mach number overpredictions by as much as 0.4% based on a simple isentropic analysis. For this reason (and those discussed earlier), the simulations do not necessarily reflect the actual tunnel flowfield; the nozzle simulations were conducted primarily to determine the thermodynamic state in the tunnel. Three axisymmetric grid levels were employed to ensure grid convergence, with the fine grid having 280×120 cells in the axial and radial directions, respectively. The coarse grids were formed by eliminating every other gridline in each direction from the finer mesh. Figure 7 shows the fine mesh with a magnified y coordinate. Note that the beginning of the test section is located at approximately $x = 2$ m.

To determine the thermal state of the flow at the test section, the nozzle was simulated assuming thermal nonequilibrium using the standard L–T formulation for vibrational relaxation. Simulation results on three grid levels (Fig. 8) indicate that the vibrational temperature freezes out very near to the plenum stagnation temperature of 633 K. Negligible differences were found between the medium and fine grid solutions.

In the "Flowfield Model" section, it was shown that for certain expanding flows, relaxation rates could be much larger than those predicted from L–T theory. To estimate the effects of this accelerated relaxation, additional nozzle simulations were performed assuming the local acceleration factor ϕ was globally fixed. Although this is certainly not the case (Fig. 2), this type of analysis is useful to gain qualitative estimates of the true relaxation rates. Figure 9 shows both translational and vibrational temperatures for acceleration factors between unity (standard L–T) and 10,000. The results clearly show that large increases in ϕ can affect the relaxation rates near the nozzle throat ($x = 0$); however, these results also show that, due to rapid expansion in the diverging section of the nozzle, the vibrational temperature freezes out very near the throat, regardless of the value of ϕ. A magnified view near the throat is shown in Fig. 10, which indicates that vibrational freezing occurs by the $x = 0.025$ m location for all cases. As shown in Fig. 2, the local acceleration

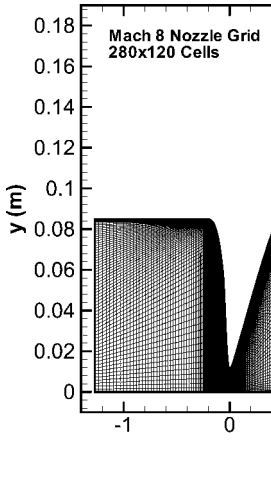

Fig. 7 Viscous nozzle grid (fine mesh) for the Mach 8 hypersonic nozzle.

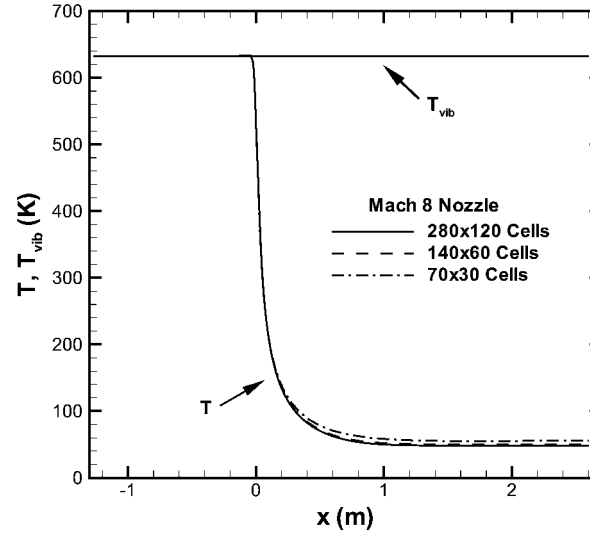

Fig. 8 Temperature distributions in nozzle assuming L–T relaxation.

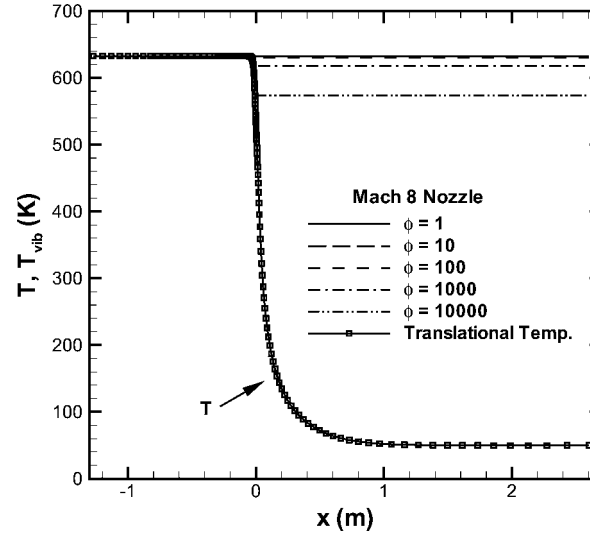

Fig. 9 Vibrational temperature in the nozzle for a number of different L–T acceleration factors ϕ: 140 × 60 cells.

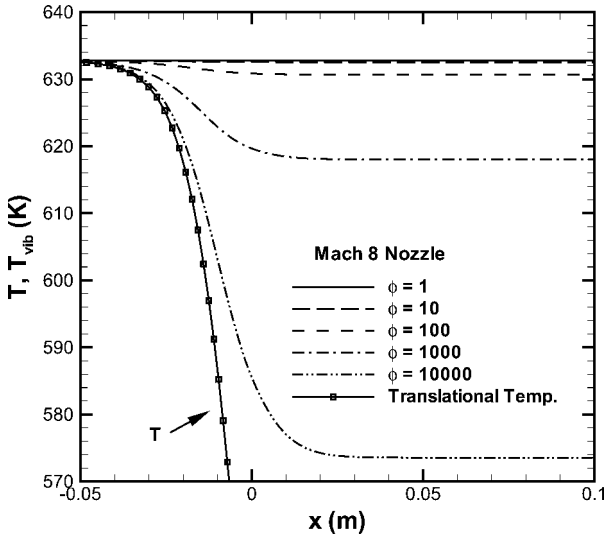

Fig. 10 Enlarged view of the vibrational temperature in the nozzle for a number of different L–T acceleration factors ϕ: 140 ×60 cells.

factor is greater than 10 only for T_{vib}/T ratios greater than 4; however, according to the $\phi = 1$ curve, the T_{vib}/T value at $x = 0.025$ m is approximately 1.5 and even smaller at the upstream locations. Thus, the profile most likely to be representative of the true behavior of the vibrational state should lie somewhere between the $\phi = 1$ and the $\phi = 10$ curves. Note that this argument assumes that the local acceleration factor for this case, with translational temperatures between 500 and 630 K, has qualitatively the same trend as the $T = 1000$ K profile given in Fig. 2. An analysis by Ruffin (private communication, September 1999) using the simplified anharmonic relaxation model, which is a higher-fidelity model than used here, on a similar nozzle geometry provides confirmation of the rapid vibrational freezing in the nozzle.

One-Dimensional Analysis

The preceding analyses indicates that the vibrational energy mode is far from equilibrium in the flow through the hypersonic wind tunnel. In this section, the effects of the vibrational nonequilibrium on the freestream conditions and the flow over the JCEAP geometry are quantified. A simple one-dimensional analysis code was written for calculating the isentropic flow in the nozzle following the work of Candler et al.[24] This code integrates the adiabatic and isentropic relationships from the nozzle plenum conditions out to a specified static pressure and assumes either vibrationally frozen at a specified temperature or thermal equilibrium via a harmonic oscillator. When this one-dimensional analysis is used, the effects of vibrational nonequilibrium on the freestream conditions can be estimated. Relative to the equilibrium case, the effects of vibrational nonequilibrium on Mach number, static pressure, static temperature, and velocity at the test section are +0.11, −0.21, −0.93, and −0.35%, respectively. Because this paper is focused on validation of the surface pressures, the primary freestream effect on the surface pressures is through the static pressure, which shows negligible effects of the vibrational nonequilibrium (0.21%).

Nonequilibrium simulations of the flow over the JCEAP geometry indicate that the freestream static pressure is low enough that, even through the normal shock wave, the flow remains thermally frozen until it reaches the wall thermal layer. Although not shown, simulation results assuming thermal nonequilibrium and thermal equilibrium gave negligible differences in surface pressure. This lack of sensitivity indicates that the thermal nonequilibrium effects impact the simulation results primarily through the freestream boundary conditions (Mach number, pressure, etc.). Thus, although the nonequilibrium effects represent bias errors in the specification of the freestream conditions (vibrational equilibrium assumed in the experimental data reduction), these errors are relatively small in the present case and can be neglected.

Although the demonstrated vibrational nonequilibrium effects did not play a major role in this study, this phenomena can be quite important in other hypersonic wind-tunnel facilities. One such example occurred recently during a code validation exercise concerning laminar, hypersonic, separated flow. As part of this effort, Holden and Harvey[25] conducted experiments on two axisymmetric configurations, a double-cone and a cylinder-cone, where shock–boundary-layer and shock–shock interactions occur. The results of this validation exercise were presented in the form of a blind comparison between the simulation predictions and the experimental data.[26] One of the main issues that arose from this validation study was that the computed surface heat fluxes (and to a lesser extent, the surface pressures) were consistently higher than the experimental data in the attached flow region upstream of the separation point. The sensitivity of the heat flux and surface pressure to the vibrational excitation in the freestream for these experiments was first demonstrated in Ref. 27. In this study, the vibrational temperature was varied from the freestream static temperature, that is, equilibrium, as assumed in the experiment, to the plenum stagnation temperature (entirely frozen flow). In this latter case, the freestream velocity was modified to produce the same total enthalpy reported in the experiment. It was later confirmed that the overprediction of the forecone heating was primarily due to the effects of vibrational freezing in the hypersonic nozzle on the freestream conditions.[28,29]

Continuum Flow Assumption

To ensure that the assumption of continuum flow is valid for the wind-tunnel nozzle in the low-pressure rapid expansion region, Bird's continuum breakdown parameter P was calculated.[30] Continuum theory breaks down for $P > 0.02$, and the maximum values calculated in the Mach 8 nozzle simulations were approximately 2×10^{-5}, thus supporting the use of continuum theory.

Outflow Boundary Condition Model

For all of the simulations presented herein, a zero gradient condition was applied at the outflow boundary. (See Fig. 1 of Ref. 6.) This boundary condition is not appropriate in the subsonic portion of the boundary layer where acoustic disturbances can travel upstream. To assess the effects of this boundary condition on the pressure distributions, an axisymmetric case was computed that included the base region. Although the model is only 0.264 m long, the domain had to be extended to 2.5 m in the axial direction to ensure supersonic flow at the outflow boundary. The wake was assumed to be laminar, and a supersonic recirculation zone appeared, consistent with earlier laminar computational studies.[31] The forebody grid used 250 × 240 cells and is similar to the 240 × 240 grid from Ref. 6 but has axial clustering at the end of the model. The base region has 340 × 360 cells with clustering near the base region and the shear layer. This base flow grid is more fully described in Ref. 32. The computations were run in parallel on six processors of the Sun Enterprise 10000 shared-memory machine.

Although the pressure does drop dramatically near the base (as shown in Fig. 11), the upstream influence is only seen for $2.5R_N$ upstream (approximately 4δ). Thus, whereas the presence of the base flow does affect the pressure at the corner, the upstream effects are limited and will not affect the experimental data comparisons because the farthest aft data location is at $x/R_N \approx 46.5$, roughly 9δ upstream of the base.

Axisymmetric Flow Assumption

The validity of the axisymmetric flow assumption was addressed by conducting full three-dimensional calculations of the JCEAP geometry including the planar slice on the aft end of the model (Fig. 1). A symmetry plane was assumed; thus, only half of the model was simulated. The three-dimensional grid was based on the 240 × 240 axisymmetric grid (considered the coarsest grid accurate enough for experimental data comparisons) and employed 105 azimuthal grid cells from the cone-symmetry plane to the slice-symmetry plane (180 deg apart). The wall normal spacing from the 240 × 240 axisymmetric grid was retained over the entire surface of the three-dimensional grid. The grid was decomposed into 144 zones and run

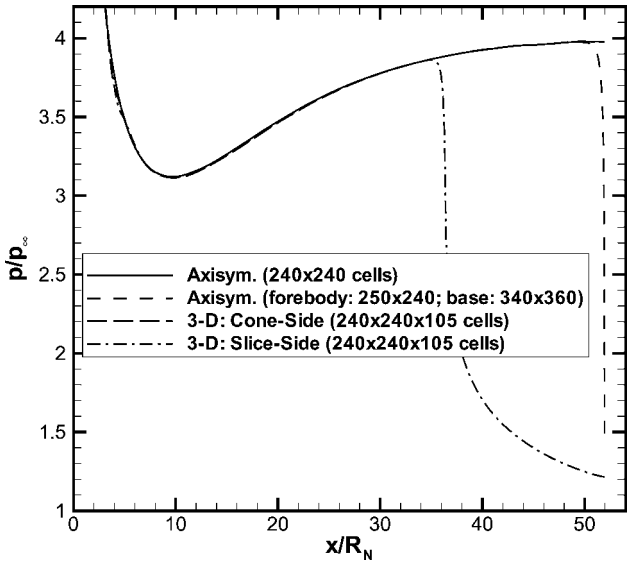

Fig. 11 Comparison of baseline simulation results with two additional computational models: axisymmetric calculation including base flow and full three-dimensional simulation including the planar slice.

in parallel on 144 processors of the Accelerated Strategic Computing Initiative Red Teraflop machine. The 6 million cell calculation converged in approximately 100 h of wall clock time.

As seen in Fig. 11, with the exception of the planar slice region, little effect is seen in the upstream region and on the cone side. Maximum differences between the baseline axisymmetric simulation and the three-dimensional calculations are approximately 0.25%. This difference occurs at approximately $x/R_N = 2$ and is probably due to grid skewing in the three-dimensional grid. This skewing is present because the axial spacing from the axisymmetric grid was maintained on the cone side, whereas the presence of the slice on the slice side required a modification to the axial clustering.

Validation of Surface Pressure Predictions

Reported Freestream Conditions

To validate the SACCARA code for attached, laminar, perfect gas, hypersonic flows, comparisons were made to the experimental surface pressure data from the JCEAP experiment.[4,5] As already mentioned, the actual JCEAP geometry has a planar slice on the aft portion of the model. Although comparisons of axisymmetric computational results with data on the slice are clearly not appropriate, the findings from the preceding subsections indicate that the data on the conical portions of the model (cone side and slice side upstream of the slice) can be used to validate the axisymmetric simulations.

Computed surface pressure distributions are compared to experimental data[4,5] in Fig. 12. The experimental measurement shown at each axial station is the mean value of all measurements taken during the experiment. The multiple measurements for each axial station were obtained from different roll orientations of the model and different axial locations of the model in the test section, as well as simple repeatability measurements taken during the entire wind-tunnel entry. The number of measurements at each axial station ranged from 48 (opposite the slice) to 768 (at $x/R_N = 16$ and 26). Statistical procedures were then applied to determine the estimated $\pm 2\sigma$ error bounds due to the presence of random error and certain correlated bias error as discussed in Refs. 2–4. As can be seen in Fig. 12, the computed pressure ratios fall consistently below the experimental data, with the poorest agreement occurring just upstream of the slice location. The maximum difference, occurring at the $x/R_N = 26$ location, is 3.3%, well outside the estimated experimental 2σ error bounds. Based on the demonstrated numerical accuracy of the simulations presented in Ref. 6, and the evaluation of the submodels, the lack of agreement between the simulation and the experiment is deemed unacceptably large and, therefore, requires further investigation.

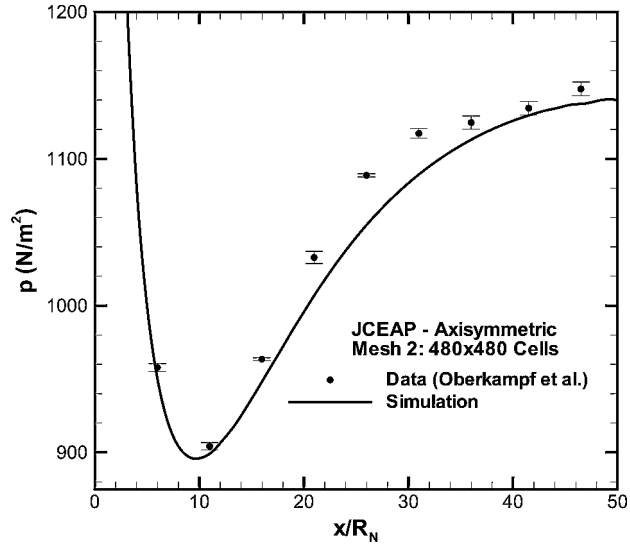

Fig. 12 Comparison of the SACCARA surface pressure results with mean JCEAP data; $p_\infty = 286.8$ N/m^2.

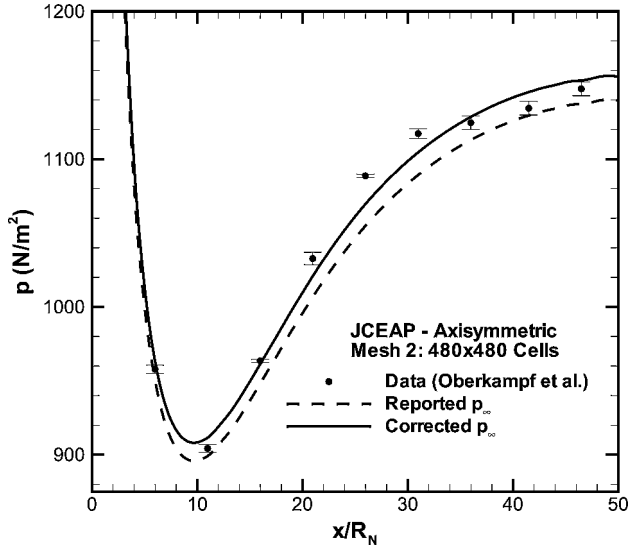

Fig. 13 Comparison of the SACCARA surface pressure results with mean JCEAP data for old and new freestream static pressure conditions; corrected $p_\infty = 290.9$ N/m^2.

Revised Freestream Conditions

After careful reexamination of the experimental data by the present authors, an error was found in the freestream static pressure originally reported in the experiment.[4,5] The nominal freestream conditions come from averaging over the freestream conditions for each of the 48 wind-tunnel runs used to obtain the surface pressure data on the JCEAP model. When the freestream static pressure values were reaveraged, the resulting static pressure (290.9 N/m^2) was found to be 1.4% larger than the static pressure initially reported in the experiment (286.8 N/m^2). The corrected freestream static pressure is shown in parentheses in Table 1.

The corrected freestream conditions were then run with the SACCARA code. Because these new conditions represent a small perturbation to the original conditions, the numerical error estimates from Ref. 9 are used. The results are shown in Fig. 13, along with the old conditions, for the 480×480 cell mesh. As expected, the effect of increasing the freestream static pressure by 1.4% is to increase the surface pressure by approximately 1.4%. The computational results with the new freestream static pressure are now in better agreement with the experimental data. When the estimated experimental uncertainty bounds and the numerical errors from Ref. 6 are accounted for,

Table 3 Experimental and computational surface pressure ratios, p/p_∞, along with experimental uncertainty and numerical error estimates for $p_\infty = 290.9$ N/m^2

Axial location (x/R_N)	Experiment (uncertainty)	Simulation: 480 × 480 cells (numerical error)
0	n/a	79.52936 (±0.13%)
0.826 (Sphere–cone tangency point)	n/a	7.60891 (±0.74%)
5.99	3.2925 (±0.29%)	3.31200 (±0.11%)
10.99	3.1083 (±0.29%)	3.13341 (±0.11%)
15.98	3.3122 (±0.10%)	3.30430 (0.11%)
20.98	3.5504 (±0.29%)	3.50938 (0.11%)
25.98	3.7425 (±0.10%)	3.67706 (0.11%)
30.99	3.8408 (±0.29%)	3.79719 (0.11%)
35.99	3.8659 (±0.40%)	3.87969 (0.11%)
41.49	3.9000 (±0.40%)	3.93747 (0.11%)
46.49	3.9450 (±0.40%)	3.96457 (0.11%)

the maximum error in surface pressure relative to the experimental data is now 1.5% at $x/R_N = 26$.

Table 3 presents the experimental and computational values for pressure ratio (p/p_∞) at all of the data locations using the corrected freestream pressure of $p_\infty = 290.9$ N/m^2. The experimental uncertainties are given for the experimental data, and numerical error estimates from Ref. 6 are given for the computational results. Also given in Table 3 are the computed pressure ratios at the stagnation point and the sphere–cone tangency point from Ref. 6, along with the associated numerical error estimates. Because of the high degree of accuracy of both the experimental data[4,5] and the simulation results,[6] Table 3 serves the dual purpose of code verification via code-to-code comparison to the computed results and code validation via comparison to the experimental data.

Although the maximum difference between the computation and experiment of 1.5%, indeed even the earlier error of 3.3%, is typically considered acceptable for engineering applications, the primary goal of this research was to develop detailed procedures for computational fluid dynamics CFD validation. As can be seen from earlier sections in this paper, one of the strategies is to carefully examine all of the assumptions and data analysis procedures of both the computational and experimental components. With regard to the experimental component, the two primary issues were the extraordinarily small $\pm 2\sigma$ estimates of experimental uncertainty and the possibility that a bias error existed in the measurements that was not included in the statistical analysis of Ref. 4. The magnitude of the $\pm 2\sigma$ uncertainty estimates at the different axial stations ranges from ±0.4 to ±0.1%. These uncharacteristically small uncertainties are simply due to the very large number of measurements made in this experiment; the uncertainty decreases as one divided by the square root of the number of measurements. As a result, the two primary experimental issues are fundamentally related: What are the possible bias errors present in the experiment that were not adequately accounted for in the statistical uncertainty analysis?

After reexamining the statistical uncertainty analysis, it was concluded that the uncertainty component due to test section flowfield nonuniformity was underestimated in the analysis. Note, however, that it was statistically demonstrated in Ref. 4 that flowfield nonuniformity was already the dominant contributor (64%) to experimental uncertainty. The best route forward, as recommended in Ref. 33 for design and execution of validation experiments, would have been to conduct an additional wind-tunnel experiment to further investigate flowfield nonuniformities. Because it was not possible to obtain additional surface pressure measurements, the next section computationally investigates the impact of flowfield nonuniformity on the surface pressure.

Flowfield Nonuniformities

When Fig. 13 is examined, there appears to be a trend in the experimental data corrected for the error in freestream static pressure that is not captured in the simulations. The anomalous trend is that experimental pressures are lower near $x/R_N = 10$ and $x/R_N = 40$ and higher near $x/R_N = 25$. In the experiment, data were taken at various azimuthal angles around the model, various roll angles, and two different axial locations in the tunnel to convert correlated bias errors due to model geometry, pressure port, and flowfield nonuniformities into random errors. However, this type of procedure will not account for the effects of axisymmetric nonuniformities, that is, nonuniformities that are functions of radial coordinate in the wind tunnel. An attempt to quantify the axisymmetric nonuniformities follows.

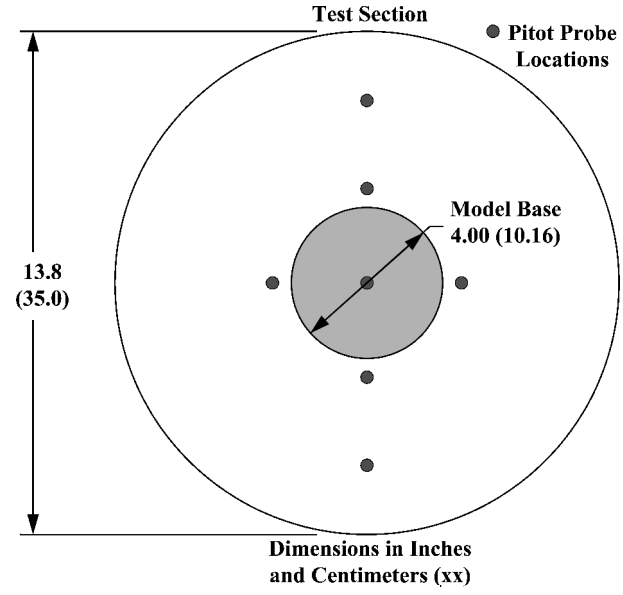

Fig. 14 Schematic of test section showing model footprint and pitot probe rake location; pitot probes spaced 2.25 in. (5.72 cm) apart.

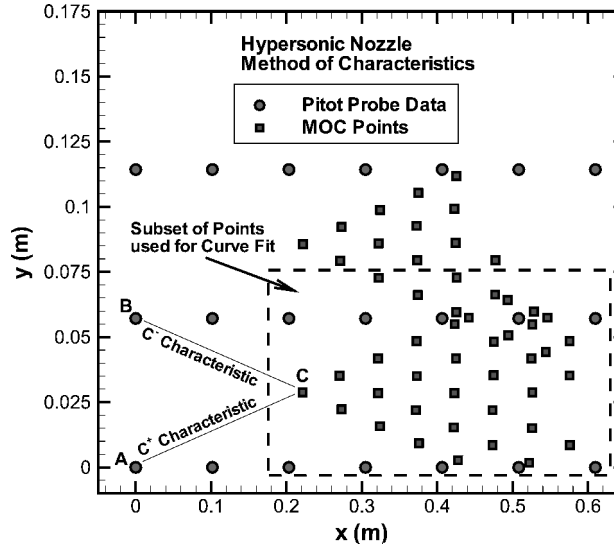

Fig. 15 Location of the pitot probes and MOC points in the hypersonic tunnel.

When the computational models discussed herein are used, the axisymmetric nonuniformities can be estimated using the flowfield calibration in the test section. A Mach number calibration was performed in 1984 using a seven-probe pitot pressure rake. The pitot probe locations are shown in Fig. 14 along with the wind-tunnel cross section (outer circle) and the JCEAP model base radius (shaded circle). The pressure field for the test section is generated in axisymmetric coordinates (x, y) by averaging the four probes located 5.72 cm away from the centerline and the two top and bottom probes located 11.4 cm from the centerline, thus, resulting in pitot data at $y = 0$, 5.72, and 11.4 cm.

The pitot probe data of interest exist at seven axial stations in the tunnel. The pitot probe locations are presented in Fig. 15, where the flow direction is left to right and the zero axial station is located at the farthest upstream pitot probe location. Only pitot data taken at

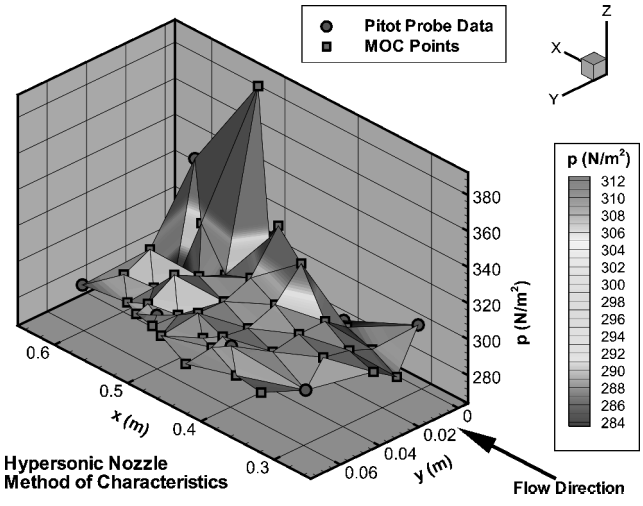

Fig. 16 Static pressures in the region used for the curve fit, both ●, pitot data and ■, MOC method points shown.

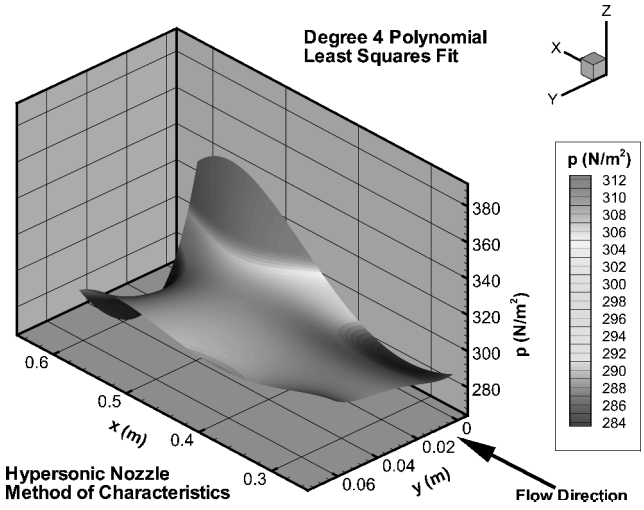

Fig. 17 Degree four polynomial least-squares fit to the pitot data and MOC points.

Reynolds numbers within 15% of the nominal test Reynolds number (6.88×10^6/m) were used, and these data were then corrected to the nominal Reynolds number. These pitot probe data were then entered into a method of characteristics code to generate additional data in the vicinity of the JCEAP model locations.

The axisymmetric method of characteristics (MOC) scheme of Hartree is employed (see Ref. 34). This MOC implementation is implicit and determines the slope of the characteristic line as the average between the origination point and the destination point. For example, the C^- characteristic shown in Fig. 15 will use the average slope found between points B and C, and the C^+ characteristic uses the average of points A and C. In this manner, the characteristic network shown in Fig. 15 is generated. The major assumption is that the radial velocity at the pitot probe locations is zero. (The pitot probe data contain no information on the flow angularity.)

Once the characteristic network is generated, there is now sufficient data resolution to include the axisymmetric nonuniformities as a nonuniform boundary condition for the simulations of the flow over the model. A three-dimensional surface plot of the surface pressure data is shown in Fig. 16. A number of expansion and compression waves are evident, with a dominant axisymmetric wave-focusing effect occurring at $x = 0.52$ m at the centerline. The subset of the pitot probe and MOC points indicated in Fig. 15 is used to construct a least-squares polynomial fit of degree four for the surface pressure. Whereas the same could be done for the other properties used for computational boundary conditions, for example, static temperature and velocities, the pressure is expected to be the first-order effect. Mathematica was employed to generate the following least-squares polynomial fit to the data:

$$p(x, y) = 211.719 + 48.0261x - 294.088y - 7.62017x^2 + 54.149xy + 71.3895y^2 + 0.442018x^3 - 2.90477x^2y - 9.05844xy^2 - 7.91981y^3 - 0.00830673x^4 + 0.0374235x^3y + 0.438069x^2y^2 - 0.916359xy^3 + 3.77575y^4 \quad (9)$$

The resulting least-squares fit from Eq. (9) is given in Fig. 17, which shows good agreement with the pitot probe and MOC data from Fig. 16.

The function $p(x, y)$ from Eq. (9) was then used to determine static pressure used as inflow boundary conditions for the simulations. Because there were two different axial testing locations used during the experiment, the least-squares fit for pressure was used to generate the boundary conditions at both locations. The simulation results accounting for axisymmetric flowfield nonuniformities at both the fore and aft model locations are presented in Fig. 18. Up until the $x/R_N = 30$ axial location, the two simulations accounting for nonuniformities obtain even better agreement

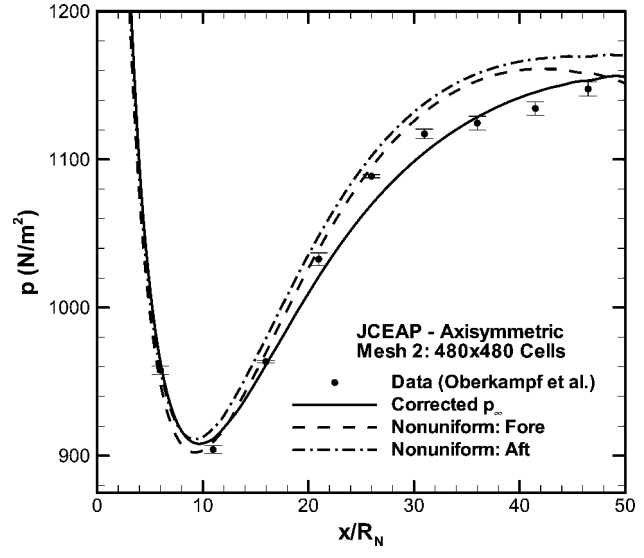

Fig. 18 Comparison of the SACCARA surface pressure results accounting for axisymmetric nonuniformities with mean JCEAP data; fore and aft test locations.

with the experimental data than the uniform flow freestream conditions. However, for $x/R_N > 30$, the nonuniform boundary simulations overpredict the pressure relative to the experimental data. Because of the assumptions used in generating the nonuniform flow computational boundary conditions, it is reasonable to assume that the true flow in the tunnel has not been accurately characterized over the entire test section. The improved level of agreement between the nonuniform flow simulations and experiment for the upstream locations on the model suggests that the axisymmetric flowfield nonuniformities may account for the remaining maximum differences between computation and experiment of 1.5%.

As the final step in the validation process, the simulation modeling errors for surface pressure relative to the experimental data are shown in Fig. 19. Also shown in Fig. 19 are the experimental uncertainties (error bars centered at zero) and the numerical error estimates from Fig. 16 of Ref. 6. The numerical errors are taken as the maximum estimated numerical error over the entire surface where experimental data are available ($6 < x/R_N < 46.5$), which in this case is 0.11%. It is clear that the correction to the freestream static pressure (curve labeled Corrected p_∞) shifts the distribution up from the originally reported conditions; however, in neither case does the character of the curves match the data. Accounting for the flowfield nonuniformities results in better agreement with the

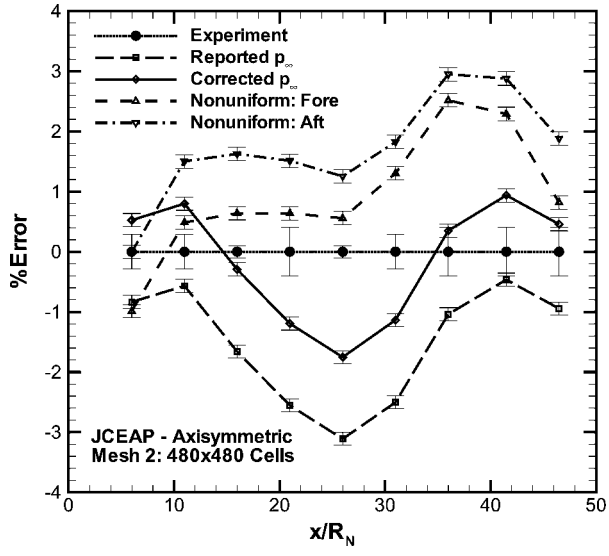

Fig. 19 Simulation error in surface pressure relative to the JCEAP experimental data.[4]

experimental data (both magnitude and character) on the upstream portions of the model. In fact, the forward testing location (where the majority of the experimental data were taken) shows agreement within 0.5% for $x/R_N < 30$.

Conclusions

The validation process requires a careful evaluation of the computational submodels as well as the assumptions made in both the simulations and the experiment. The computational submodels for the transport properties, equation of state, vibrational nonequilibrium, and the base-flow boundary condition were evaluated. In addition, the assumptions made in the computations regarding continuum flow and axial symmetry were found to be valid for this case. The calibration of the flow in the test section of the wind tunnel assumed that the flow was in thermal equilibrium. To evaluate this assumption, simulations of the hypersonic wind-tunnel nozzle were performed. It was determined that the flow was vibrationally frozen near the plenum temperature; however, bias errors arising from the assumption of thermal equilibrium were found to have a negligible impact on the surface pressure results.

Through a reexamination of the experimental data, a bias error of 1.4% was found in the freestream static pressure quoted in the experiment. This bias error arose from an error in averaging the static pressure values over the 48 experimental runs used to obtain the surface pressure data. Correcting for this bias error resulted in improved agreement between simulation and experiment. When both experimental uncertainty and the numerical error in the simulations are accounted for, the agreement for surface pressure using the corrected freestream conditions was a maximum of 1.5% over the entire length of the model.

The findings from Ref. 4 show that flowfield nonuniformities are the largest contributor to the experimental uncertainty. Further examination of the JCEAP experimental data revealed that axisymmetric nonuniformities were not taken into account during the experimental uncertainty analyses. Because additional experimental studies of the axisymmetric flowfield nonuniformities were not possible, the effects of these nonuniformities were investigated computationally. Pitot pressures from an earlier Mach number calibration of the wind tunnel were used, along with the axisymmetric MOC, to obtain detailed information on freestream static pressure in the vicinity of the model testing locations. These nonuniformities were then used as detailed inflow boundary conditions for the simulations. Accounting for the axisymmetric flowfield nonuniformities resulted in agreement within 0.5% on the upstream portion of the model; however, increased resolution in the experimental pitot probe data is needed to characterize accurately the true nonuniformities in the tunnel. Including detailed boundary condition information to be used as an input to the simulation represents the next level of code validation.

One of the difficulties that had to be overcome in resolving the differences in the current validation exercise was the time span (approximately seven years) between the experiment and the current computations. As stressed in Ref. 33, validation experiments must be carried out in conjunction with computational analyses. Not only can this aid in the design of the experiment, but it also provides an additional check on the assumptions made, both in the experiment and in the computations. From the present work, it is concluded that a recalibration of the Sandia hypersonic wind tunnel is needed. This recalibration should use frozen flow theory instead of assuming the flow is in thermal equilibrium and should have a much finer spatial resolution at the test locations to provide detailed boundary conditions to be used as inflow conditions for modeling and simulation. The authors believe that as more detailed validation experiments are conducted, this conclusion will remain true for most wind tunnels.

Acknowledgments

This work was supported by Sandia National Laboratories and the Department of Energy's Accelerated Strategic Computing Initiative. Sandia is a multiprogram laboratory operated by Sandia Corporation, a Lockheed Martin Company, for the U.S. Department of Energy under Contract DE-AC04-94AL85000. The authors thank Daniel Aeschliman who, along with the second author, provided the experimental data utilized in this paper. We also thank Stephen Ruffin of the Georgia Institute of Technology for his consultations regarding vibrational nonequilibrium and John Henfling of Sandia National Laboratories, who provided valuable information on the Joint Computational/Experimental Aerodynamics Program experiments. Finally, we thank Frederick Blottner of Sandia National Laboratories for his insight into the effects of vibrational nonequilibrium.

References

[1]*Guide for the Verification and Validation of Computational Fluid Dynamics Simulations*, G-077-1998, AIAA, Reston, VA, 1998, p. 3.

[2]Oberkampf, W. L., Aeschliman, D. P., Tate, R. E., and Henfling, J. F., "Experimental Aerodynamic Research on a Hypersonic Vehicle," Sandia National Labs., Rept. SAND 92-1411, Albuquerque, NM, Jan. 1993.

[3]Oberkampf, W. L., and Aeschliman, D. P., "Joint Computational/Experimental Aerodynamics Research on a Hypersonic Vehicle, Part 1: Experimental Results," *AIAA Journal*, Vol. 9, No. 3, 1995, pp. 432–437.

[4]Oberkampf, W. L., Aeschliman, D. P., Henfling, J. F., and Larson, D. E., "Surface Pressure Measurements for CFD Code Validation in Hypersonic Flow," AIAA Paper 95-2273, June 1995.

[5]Oberkampf, W. L., Aeschliman, D. P., Henfling, J. F., Larson, D. E., and Payne, J. L., "Surface Pressure Measurements on a Hypersonic Vehicle," AIAA Paper 96-0669, Jan. 1996.

[6]Roy, C. J., McWherter-Payne, M. A., and Oberkampf, W. L., "Verification and Validation for Laminar Hypersonic Flowfields, Part 1: Numerical Error Assessment," *AIAA Journal*, Vol. 41, No. 10, 2003, pp. 1934–1943.

[7]Wong, C. C., Soetrisno, M., Blottner, F. G., Imlay, S. T., and Payne, J. L., "PINCA: A Scalable Parallel Program for Compressible Gas Dynamics with Nonequilibrium Chemistry," Sandia National Labs., Rept. SAND 94-2436, Albuquerque, NM, 1995.

[8]Wong, C. C., Blottner, F. G., Payne, J. L., and Soetrisno, M., "Implementation of a Parallel Algorithm for Thermo-Chemical Nonequilibrium Flow Solutions," AIAA Paper 95-0152, Jan. 1995.

[9]"INCA User's Manual," Ver. 2.0, Amtec Engineering, Inc., Bellevue, WA, 1995.

[10]Steger, J. L., and Warming, R. F., "Flux Vector Splitting of the Inviscid Gasdynamic Equations with Applications to Finite Difference Methods," *Journal of Computational Physics*, Vol. 40, 1981, pp. 263–293.

[11]Yee, H. C., "Implicit and Symmetric Shock Capturing Schemes," NASA TM-89464, May 1987.

[12]Walker, M. M., and Oberkampf, W. L., "Joint Computational/Experimental Aerodynamics Research on a Hypersonic Vehicle, Part 2: Computational Results," *AIAA Journal*, Vol. 30, No. 8, 1992, pp. 2010–2016.

[13]McBride, B. J., Gordon, S., and Reno, M. A., "Coefficients for Calculating Thermodynamic and Transport Properties of Individual Species," NASA TM 4513, Oct. 1993.

[14]Gnoffo, P. A., Gupta, R. N., and Shinn, J. L., "Conservation Equations and Physical Models for Hypersonic Air Flows in Thermal and Chemical Nonequilibrium," NASA TP-2867, Feb. 1989.

[15]Millikan, R. C., and White, D. R., "Systematics of Vibrational Relaxation," *Journal of Chemical Physics*, Vol. 39, No. 12, 1963, pp. 3209–3213.

[16]Bray, K. N. C., "Chemical and Vibrational Nonequilibrium in Nozzle Flows," *Nonequilibrium Flows, Part II*, Marcel Dekker, New York, 1970, pp. 67–68.

[17]Ruffin, S. M., "Prediction of Vibrational Relaxation in Hypersonic Expanding Flows, Part 1: Model Development," *Journal of Thermophysics and Heat Transfer*, Vol. 9, No. 3, 1995, pp. 432–437.

[18]Ruffin, S. M., "Prediction of Vibrational Relaxation in Hypersonic Expanding Flows, Part 2: Results," *Journal of Thermophysics and Heat Transfer*, Vol. 9, No. 3, 1995, pp. 438–445.

[19]Van Wylen, G. J., and Sonntag, R. E., *Fundamentals of Classical Thermodynamics*, 3rd ed., SI Ver., Wiley, New York, 1985, p. 44.

[20]Cengal, Y. A., and Boles, M. A., *Thermodynamics: An Engineering Approach*, 2nd ed., McGraw–Hill, New York, 1994, pp. 635–644.

[21]Keyes, F. G., "A Summary of Viscosity and Heat-Conduction Data for He, A, H_2, O_2, CO, CO_2, H_2O, and Air," *Transactions of the ASME*, July 1951, pp. 589–596.

[22]Incropera, F. P., and DeWitt, D. P., *Fundamentals of Heat and Mass Transfer*, 3rd ed., Wiley, New York, 1990, p. A18.

[23]Weast, R. C. (ed.), *CRC Handbook of Chemistry and Physics*, CRC Press, Boca, Raton, FL, 1984, pp. B-363, E-3.

[24]Candler, G. V., Nompelis, I., Druguet, M.-C., Holden, M. S., Wadhams, T. P., Boyd, I. D., and Wang, W.-L., "CFD Validation for Hypersonic Flight: Hypersonic Double-Cone Flow Simulations," AIAA Paper 2002-0581, Jan. 2002.

[25]Holden, M. S., and Harvey, J. K., "Code Validation Study of Laminar Shock/Boundary Layer and Shock/Shock Interactions in Hypersonic Flow, Part A: Experimental Measurements," AIAA Paper 2001-1031, Jan. 2001.

[26]Harvey, J. K., Holden, M. S., and Wadhams, T. P., "Code Validation Study of Laminar Shock/Boundary Layer and Shock/Shock Interactions in Hypersonic Flow, Part B: Comparison with Navier–Stokes and DSMC Solutions," AIAA Paper 2001-1031, Jan. 2001.

[27]Roy, C. J., Bartel, T. J., Gallis, M. A., and Payne, J. L., "DSMC and Navier–Stokes Predictions for Hypersonic Laminar Interacting Flows," AIAA Paper 2001-1030, Jan. 2001.

[28]Candler, G. V., Nompelis, I., Druguet, M.-C., Holden, M. S., Wadhams, T. P., Boyd, I. D., and Wang, W.-L., "CFD Validation for Hypersonic Flight: Hypersonic Double-Cone Flow Simulations," AIAA Paper 2002-0581, Jan. 2002.

[29]Holden, M. S., Wadhams, T. P., Harvey, J. K., and Candler, G. V., "Comparisons Between Measurements in Regions of Laminar Shock Wave Boundary Layer Interaction in Hypersonic Flows with Navier–Stokes and DSMC Solutions," AIAA Paper 2002-0435, Jan. 2002.

[30]Bird, G. A., *Molecular Gas Dynamics and the Direct Simulation of Gas Flows*, Clarendon, Oxford, 1994, p. 4.

[31]Grasso, F., and Pettinelli, C., "Analysis of Laminar Near-Wake Hypersonic Flows," *Journal of Spacecraft and Rockets*, Vol. 32, No. 6, 1995, pp. 970–980.

[32]Roy, C. J., McWherter-Payne, M. A., and Oberkampf, W. L., "Verification and Validation for Laminar Hypersonic Flowfields," AIAA Paper 2000-2550, June 2000.

[33]Aeschliman, D. P, and Oberkampf, W. L., "Experimental Methodology for Computational Fluid Dynamics Code Validation," *AIAA Journal*, Vol. 36, No. 5, 1998, pp. 733–741.

[34]Owczarek, J. A., *Fundamentals of Gas Dynamics*, International Textbook, Scranton, PA, 1964, pp. 472–481.

G. V. Candler
Associate Editor